Multi-layer Seismic Anisotropy Beneath Greenland

Erica Mae Nathan[1], Anant Hariharan[1], Darien Florez[1], and Karen M Fischer[1]

[1]Brown University

December 31, 2020

Abstract

Seismic anisotropy provides insight into past episodes of lithospheric deformation and the orientations of strain in the underlying asthenosphere. The Greenland mantle has played host to a rich history of tectonic processes, including multiple orogenies and plume-lithosphere interactions. This study presents new measurements of SKS splitting that reveal strong variations in fast polarization direction with back-azimuth that are consistent across Greenland, including at stations where splitting measurements have not previously been reported. We compared observed fast polarization directions to the predictions of two-layer models with olivine-orthopyroxene anisotropy. The family of models which provides acceptable misfits at 95% confidence indicates an upper layer olivine a-axis azimuth of 226 +/- 2.9{degree sign} and a lower layer olivine a-axis azimuth of 124 +/- 2.7{degree sign} and non-zero axis dips are required. These models are consistent with asthenospheric anisotropy aligned approximately parallel to the direction of plate motion and lithospheric anisotropy due to Proterozoic and Archean orogenic fabrics.

Multi-layer Seismic Anisotropy Beneath Greenland

Erica Nathan[1,2], Anant Hariharan[1,2], Darien Florez[1], Karen M. Fischer[1]

[1]Department of Earth, Environmental, and Planetary Sciences, Brown University, Providence, RI, USA
[2]These authors contributed equally to this work.

Key Points:

- 299 new *KS shear wave splitting measurements made using broadband stations across Greenland
- Variations of fast direction with back-azimuth can be explained by two layers of anisotropy which are consistent across Greenland
- Lower layer consistent with asthenospheric shear; upper layer consistent with past lithospheric orogenic deformation

Corresponding author: Erica Nathan, erica_nathan@brown.edu

Abstract

Seismic anisotropy provides insight into past episodes of lithospheric deformation and the orientations of strain in the underlying asthenosphere. The Greenland mantle has played host to a rich history of tectonic processes, including multiple orogenies and plume-lithosphere interactions. This study presents new measurements of SKS splitting that reveal strong variations in fast polarization direction with back-azimuth that are consistent across Greenland, including at stations where splitting measurements have not previously been reported. We compared observed fast polarization directions to the predictions of two-layer models with olivine-orthopyroxene anisotropy. The family of models which provides acceptable misfits at 95% confidence indicates an upper layer olivine a-axis azimuth of $226\pm2.9°$ and a lower layer olivine a-axis azimuth of $124\pm2.7°$ and non-zero axis dips are required. These models are consistent with asthenospheric anisotropy aligned approximately parallel to the direction of plate motion and lithospheric anisotropy due to Proterozoic and Archean orogenic fabrics.

Plain Language Summary

Measurements of seismic anisotropy (the direction-dependent variation of seismic wavespeed) provide useful information about the orientation of deformation in the Earth. We measured seismic anisotropy using shear waves refracted through the outer core and recorded by stations in Greenland. Due to new stations and data, this study includes more measurements of the effects of anisotropy than previously possible. We show that a model with two layers of anisotropy explains dominant patterns in the fast vibration direction of the shear waves as a function of the angle at which they approach each station. We suggest that the lower layer reflects deformation in the asthenospheric mantle induced by the motion of the plate above, and the shallow layer reflects coherent deformation in the continental lithosphere of Greenland due to its history of plate collisions.

1 Introduction

Nearly all of Greenland's surface geology is inaccessible because it is covered by the Greenland Ice Sheet. Therefore, geophysical investigations are especially important in furthering our understanding of Greenland's subglacial lithospheric structure. Greenland is a region of interest as its lithosphere contains cratonic material and records the history of Archean, Proterozoic, and Paleozoic orogenies, and also could provide insight into the history of the Iceland plume (e.g Henriksen et al., 2009).

The majority of Greenland is Precambrian and has been modified by multiple tectonic (orogenic and rifting) events (e.g Henriksen et al., 2009). Of particular note is the Trans-Hudson Orogeny which was a widespread set of plate collisions that helped to build Laurentia around 1.8 Ga (e.g St-Onge et al., 2009). Orogenic belts from this event can be found across North America; in Greenland this includes the Rinkian and Nagssugtoqidian belts that bound major crustal blocks (e.g Antonijevic & Lees, 2018; Dahl-Jensen et al., 2003; Henriksen et al., 2009). During the Silurian, the continent-continent collision of Laurentia and Baltica developed the Eastern Greenland Caledonides, resulting in complex thrust architecture along the Eastern coast (e.g Dawes, 2009; Higgins & Leslie, 2000). More recently, Greenland has been modified volcanically and thermally by the passage of the Iceland plume underneath Greenland between 70-40 Ma (e.g Lawver & Muller, 1994). However, studies differ regarding the exact path of the plume under Greenland and its effects on the overlying lithosphere (Braun et al., 2007; Forsyth et al., 1986; Lawver & Muller, 1994; Steffen et al., 2018; Steinberger et al., 2019). Regional-scale seismic imaging has helped elucidate this tectonic history, constrain the temperature and composition of the Greenland mantle, and interrogate plume-lithosphere interactions. Surface-wave tomography (Darbyshire et al., 2018; Lebedev et al., 2018; Levshin et al., 2001) has detected thick depleted cratonic mantle lithosphere and lithospheric structures modified by multiple tectonic events. H-K stacking and synthetic modeling of receiver functions have helped to constrain regional crustal thickness and composition (Dahl-Jensen et al., 2003; Kumar et al., 2005, 2007). Images from body-wave tomography (Toyokuni et al., 2020) show a NW-SE low-velocity anomaly within the mantle, coincident with heat flow anomalies interpreted as evidence for plate movement over the Iceland plume. Surface wave tomography (Levshin et al., 2017; Lebedev et al., 2018; Mordret, 2018; Pourpoint et al., 2018) has also been used to identify this thermal signature. In the mantle, a common source of anisotropy is the lattice preferred orientation of minerals such as olivine and orthopyroxene; in conditions where the mantle is relatively dry and/or low stress, shear wave splitting fast polarization directions are thought to align approximately parallel to the direction of horizontal flow (Karato et al., 2008; Long & Becker, 2010). Shape preferred orientation of velocity heterogeneity can also cause anisotropy (Holtzman et al., 2003).

Relatively few studies of seismic anisotropy exist for the mantle beneath Greenland. Azimuthal anisotropy in global-scale images (Ekström, 2011; Schaeffer et al., 2016) is difficult to interpret due to the coarse parameterization of these models, which provide only a small number of data points in Greenland. A regional-scale surface-wave study (Darbyshire et al., 2018) shows weak anisotropy at shallow mantle depths with a NW-SE fast direction beneath the central latitudes of Greenland and NE-SW fast directions in the far north and south, but only provides constraints in the uppermost mantle. Previous shear wave splitting measurements are predominantly N-NE in southern Greenland, and more variable elsewhere (e.g Ucisik et al., 2008). A lateral gradient in anisotropy near the southern coast of Greenland has also been measured with quasi-love waves (Servali et al., 2020).

Shear-wave splitting arises when anisotropic media polarize shear wave particle motions that travel at different velocities, and the polarization direction of the fast shear wave (Φ) and the time delay (δt) between the two split waves measured at the receiver are commonly used to characterize the anisotropy. The presence of multiple layers of anisotropy, with different a-axis azimuth, a-axis plunge, and/or strength result in back-azimuthal variation of the measured splitting parameters. When detected, back-azimuthal variations of apparent splitting parameters are a useful tool for measuring the variation of anisotropy with depth (e.g. Savage & Silver, 1993; Silver & Savage, 1994; Levin et al., 1999). A range of approaches have been applied to this problem, including exploration of the large model space using the neighbourhood algorithm (e.g. Wookey, 2012; Yuan & Levin, 2014). Grid searches through model parameter space have also been used to constrain a-axis azimuth, plunge, and anisotropy strength (Abt et al., 2010). Forward modeling that parameterizes the anisotropy in each layer with a fast polarization direction and splitting time is also sometimes employed, reducing the parameter space (e.g Aragon et al., 2017; Hammond et al., 2014; Wookey, 2012) In a limited number of cases, tomographic approaches have been applied to shear-wave splitting from local (Abt & Fischer, 2008; Abt et al., 2009; Calixto et al., 2014) and teleseismic events (Long et al., 2008; Mondal & Long, 2020).

Although prior studies have measured shear wave splitting in Greenland (Clement et al., 1994; Helffrich et al., 1994; Vinnik et al., 1992; Ucisik et al., 2005, 2008), clear variations in splitting parameters with back-azimuth diagnostic of multiple layers of anisotropy have not been resolved (e.g Ucisik et al., 2008). In this study, we measure shear wave splitting across Greenland using decades of new data and dozens of new stations, observe systematic variations in fast polarization direction with back-azimuth, and model these patterns with two-layer anisotropy.

2 Data and Methods

2.1 Data

We measured shear-wave splitting fast polarizations and delay times from *KS phases using a new dataset collected from 27 stations deployed on the Greenland ice sheet and coast, as well as stations on Ellesmere Island (ALE) and on Jan Mayen Island (JMIC) (Table S1). Seismic data used in this analysis were acquired at broadband stations, which were deployed for different periods of time (Table S1), ranging from four months (for stations part of temporary deployments) to nearly 30 years. Stations include those from network codes DK (the Danish Seismological Network), GE (GEOFON), XF (GLISN), G (GEOSCOPE), CN (Canadian National Seismograph Network) and II (the IRIS/USGS Global Seismographic Network) (Table S1). Station spacing varies dramatically, from more than 200 km on the ice sheet to less than 50 km on the coast, with stations mostly distributed along the coast. We employed BH* channels sampled at 100 Hz. We selected earthquakes of magnitude greater than 6.0, between epicentral distances of 90° and 130° from each station.

2.2 Measurement Methods

To measure shear-wave splitting, we employed the SplitLab software (Wüstefeld et al., 2008). We filtered waveforms between 0.01 and 0.1 Hz before manually inspecting and windowing data around the *KS phase. We report results of the transverse-component minimization method (Silver & Chan, 1991), although we only retained measurements whose uncertainties overlapped those from eigenvalue minimization. We imposed several other criteria to distinguish a measurement as high quality (e.g. Fig. 1): the *KS phase is a clear arrival with a signal-to-noise ratio ≥ 2 on the Q component; *KS phases (isolated or coincident) behave like a split *KS phase, i.e. the energy on the transverse component decreases and elliptical particle motion becomes linear when splitting is removed from the waveforms; the 95% error surfaces for the transverse-component minimization method and eigenvalue minimization method are close to an ellipse; the un-

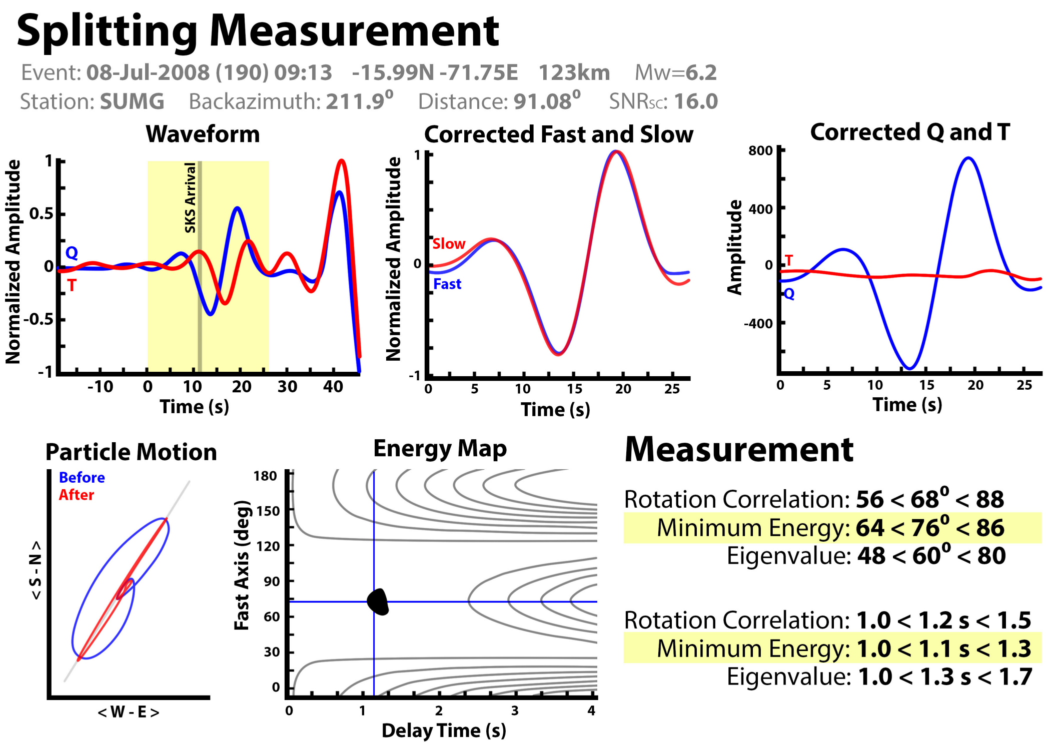

Figure 1. Example of a high quality splitting measurement obtained using SplitLab (Wüstefeld et al., 2008). Upper left: Q and T components of initial waveforms. An SKS phase is highlighted in the yellow window. Upper center: SKS phase waveform on fast and slow polarization components, shifted to remove the splitting lag time. Upper right: The shifted waveform components on the Q and T components. Lower left: Horizontal components of the SKS phase before (blue) and after (red) the splitting lag time was removed. Lower center: Surface of energy on the T component as a function of trial splitting fast direction and delay time. Splitting parameters within 95% confidence of the best-fitting values lie within the shaded contour. Lower right: fast direction and splitting time (with uncertainties) for each of the measurement methods.

certainty range in splitting time does not overlap zero nor does it exceed 4 seconds; the uncertainty in fast direction is less than ±30° for the transverse-component minimization method.

3 Results

3.1 Shear-wave Splitting Results

We measured a total of 299 high quality shear wave splitting measurements (Table S2). At many stations, there is significant variation in the measured fast directions with back-azimuth (Fig. 2, Fig. S1). In particular, the stations with the largest number of measurements (e.g. ALE, NEEM, SCO) all show clear variation in fast direction with back-azimuth. For example, at station NEEM (Fig. 3a), fast directions span 27°–171°. At other stations, the fast directions are clustered around a single value (e.g. NE6, TULEG, KULLO, DAG, ISOG). However, at some stations the distribution of measurements with back-azimuth is insufficient to determine whether back-azimuthal variation in fast direction exists. In addition, there is little geographic coherence in mean fast direction between stations (Fig. 2, Fig. S1).

To examine whether measurements at individual stations can be fit by a single layer of anisotropy, we determined the single horizontal olivine a-axis orientation whose predicted shear-wave splitting fast directions produce the minimum summed circular misfit when compared to the observed fast directions at the station. Our measurements fall into three back-azimuth ranges of width 120°. If the maximum misfit (with respect to the best-fitting a-axis orientation) to a single observation in any cluster is greater than 30°, we deem the fast directions as not fit by a single layer. Stations are deemed ambiguous if the maximum circular misfit is less than 30° for all observed fast directions, but data do not exist in all three back-azimuth bins, which could result in under-sampling of the predictions of an underlying two-layer anisotropy pattern. Using this definition, only stations NE6 and ISOG are consistent with a single layer of anisotropy (Fig. 2).

In addition, when all fast polarizations are plotted together (Fig. 3b), their overall pattern of fast direction variation with back-azimuth is broadly consistent, including stations which can and cannot be fit by a single layer of anisotropy (Fig. 2, Fig. S1). This broad pattern of fast direction variation in back-azimuth (Fig. 3b) persists in regional sub-groups of stations, for example those north and south of 70° N (Fig. 3b).

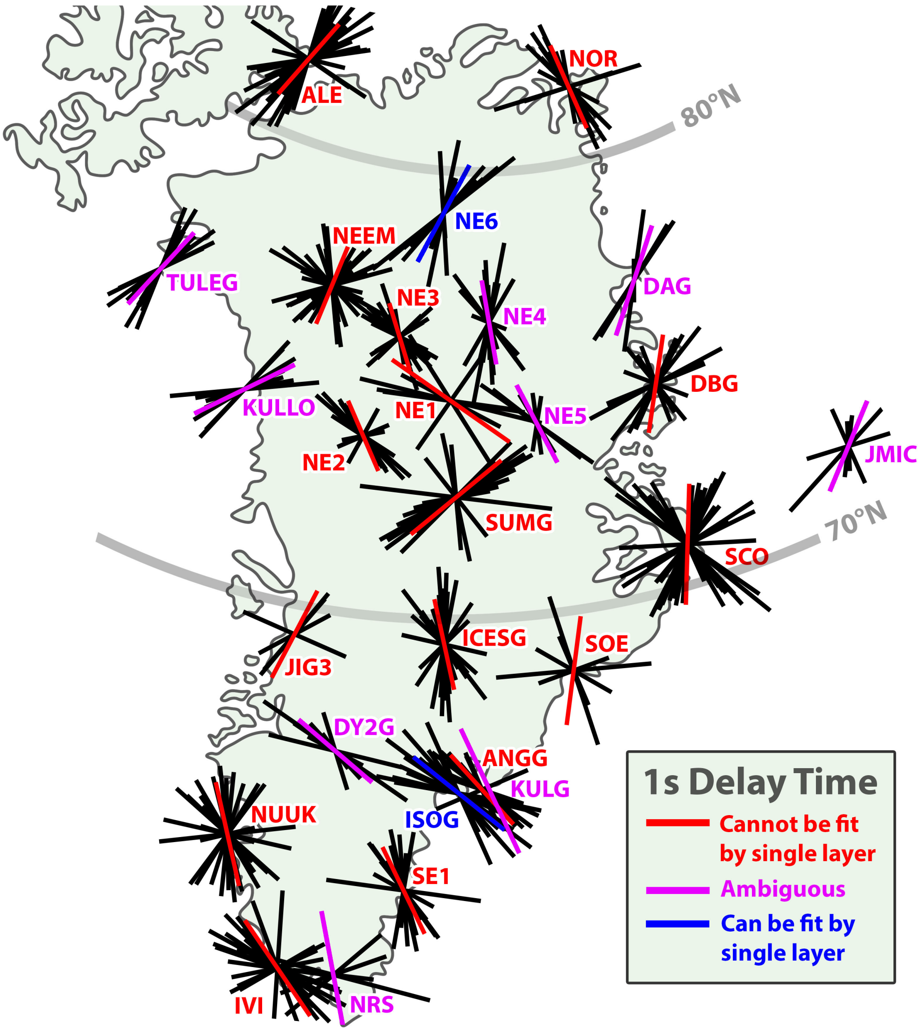

Figure 2. Map of individual splitting measurements (black lines) and average fast direction (colored lines) measured at each station. Color shows classification of whether the fast directions at the station can or cannot be fit by a single layer of anisotropy. The length of the lines corresponds to splitting time; the time scale appears in the legend.

3.2 Modeling Two Layers of Anisotropy

To constrain the variation of anisotropy with depth implied by the observed variation of shear-wave splitting fast directions with back-azimuth, we compare observed fast directions to the predictions of two-layer anisotropy models. We assume an isotropic crust of thickness 40 km (Darbyshire et al., 2018), an anisotropic mantle lithosphere between 40 km and 150 km, and an anistropic asthenosphere between 150 and 300 km. The mantle lithosphere thickness is based on thermally defined lithospheric thickness values for

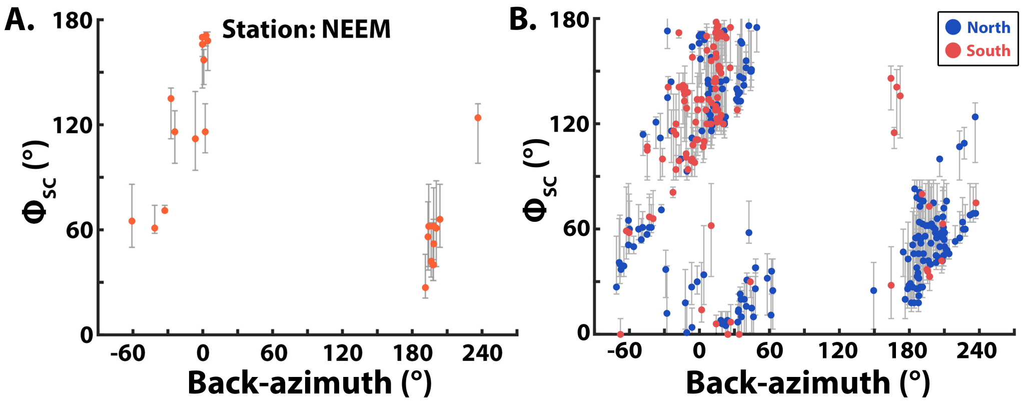

Figure 3. a) Fast directions versus back-azimuth at station NEEM. Significant variation in fast direction occurs which cannot be explained by a single layer of anisotropy. Plots for all other stations can be found in Fig. S1. b) All measurements of fast direction as a function of back-azimuth for our study area separated into northern ($< 70°$N) and southern ($< 70°$ N) groups based on station latitude. N=299.

Greenland (Steinberger & Becker, 2018). To define the tensor of anisotropic elastic coefficients, we assumed a mantle composed of 70% olivine and 30% orthopyroxene. The model has six free parameters: olivine a-axis azimuth (θ) and plunge (δ), and anisotropy strength (α) in each of the two layers. Anisotropy strength is defined as the percentage of total single crystal anisotropy. In other words, 100% anisotropy would be the elastic coefficients for pure olivine and orthopyroxene, aligned with respect to each other so that the a-axis of olivine is parallel to the c-axis of orthopyroxene, and the b-axis of olivine is parallel to the a-axis of orthopyroxene (Mainprice & Silver, 1993)

We predict shear-wave splitting parameters for each back-azimuth in the observed splitting dataset using the approximate particle motion perturbational method (Fischer et al., 2000); this approach has been shown to match results generated using pseudospectral synthetics (Hung & Forsyth, 1998). The code rotates and time-shifts an initial linear wavelet of period 10 s using the Christoffel matrix for the anisotropy in the lower layer, and then rotates and time-shifts the resulting particle motion for the anisotropy in the upper layer. Shear-wave splitting parameters are then measured from the synthetic waveform using the eigenvalue minimization method (Silver & Chan, 1991), which for the noise-free synthetics used in the modeling yields identical results to the transverse energy minimization method that was applied to the data.

Because of the non-linear relationship of anisotropy model parameters to shear-wave splitting predictions, we employ a grid-search approach to determine the best-fitting model parameters. Due to the large number of model parameter combinations, we first compare the observed fast directions to predicted fast directions from a more coarsely sampled grid of parameters, and then implement a finer grid search around the minima resolved from the coarser grid. In the coarse grid search, a-axis azimuth varies in increments of 10° between 0°-360° from north, a-axis plunge varies in increments of 10° between 0°-50° from horizontal, and the strength of anisotropy varies in increments of 10% between 0%-50%. In the finer grid search, we probe a-axis azimuths in increments of 2° in a range ±20° away from the best-fitting value from the coarse grid search, and probe dip and strength along the same spacing as in the coarse grid search.

Using the measurements of fast directions from all stations (Fig. 3b, Table S2), the coarse grid search yields a global minimum RMS misfit of 2.81 at $\theta_{deep} = 130°$, $\delta_{deep} = 40°$, $\alpha_{deep} = 50\%$; $\theta_{shallow} = 230°$, $\delta_{shallow} = 30°$, $\alpha_{shallow} = 40\%$ (Fig. 4). There are other local minima, but these do not minimize misfit. The finer grid search finds a better-fitting model with a misfit of approximately 2.26 (Fig. 4). The best-fitting parameters for the finer grid search are $\theta_{deep} = 124°$, $\delta_{deep} = 50°$, $\alpha_{deep} = 50\%$; $\theta_{shallow} = 226°$, $\delta_{shallow} = 20°$, $\alpha_{shallow} = 40\%$. We use an F-test (Snecdecor & Cochran, 1991) to determine the family of models that fit the observations within the 95% confidence limits of the best-fitting model.

From the fine grid search, we find a total of 39 models which satisfy the 95% confidence interval constraint, and adequately predict the large-scale variation of fast axis with back-azimuth (Fig. 5, left). As the width of the parameter histograms (Fig. 5, right) indicate, our grid search places robust constraints on the a-axis azimuths in the upper and lower layers. Acceptable a-axis azimuths in the upper layer vary from 222° to 232°, and in the lower layer from 120° to 130°. A-axis plunge in the lower layer is at 50°, while acceptable values of a-axis plunge in the upper layer range from 10° to 30°. Among the parameters we probe in our grid search, the strength of anisotropy in each layer is the least well constrained. Unlike dip or layer a-axis orientation, it does not result in sharp discontinuities in the variation of fast axis with back-azimuth, and the model misfits are thus the least sensitive to it. Furthermore, the strength of anisotropy trades off with the thickness of each layer, as well as with the a-axis plunge (Abt et al., 2010). Nonetheless, the large values of strength highlight distinct and strong anisotropy in each layer.

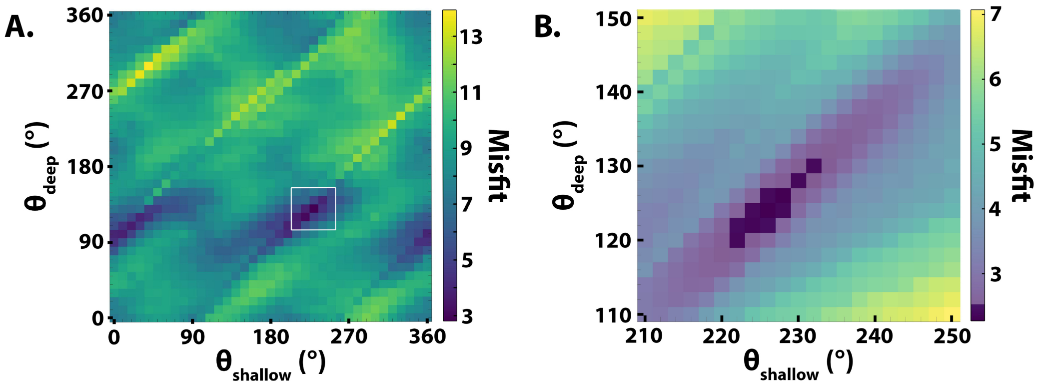

Figure 4. a): Misfit surface along a constant $\delta_{deep} = 40°$, $\alpha_{deep} = 50\%$, $\delta_{shallow} = 30°$, and $\alpha_{shallow} = 40\%$ showing variation in misfit as a function of θ_{deep} and $\theta_{shallow}$. The best fitting model from the coarse grid search is at $\theta_{deep} = 130°$, $\delta_{deep} = 40°$, $\alpha_{deep} = 50\%$; $\theta_{shallow} = 230°$, $\delta_{shallow} = 30°$, $\alpha_{shallow} = 40\%$ with a misfit of 2.8145. This model does not satisfy the F-test criterion corresponding to the finer grid search. The a-axis range probed in the finer grid search, which encloses the best-fitting model from the coarse grid search, is outlined in white. b): As in left, but for the finer grid search. This misfit surface is along constant $\delta_{deep} = 50°$, $\alpha_{deep} = 50\%$, $\delta_{shallow} = 20°$, and $\alpha_{shallow} = 40\%$. The darkened region in the right panel indicates parameters that lie within the 95% confidence F-test limits of the best-fitting model.

The delay times we measure exhibit significant scatter (Fig S2). Due to this, back-azimuthal variation in the delay times is not discernable and the distribution of delay times is fairly unimodal, centered on a mean of ≈ 1.7s, albeit with a large standard deviation of ≈ 0.5s. As a result, we follow the convention used in many mantle-scale shear wave splitting studies (Aragon et al., 2017; Hammond et al., 2014; Dubé et al., 2020) and do not attempt to incorporate predictions of variations in delay times in our final grid searches for the best-fitting model parameters in each layer.

To investigate how the non-uniform back-azimuthal sampling of fast direction patterns affects the resolvability of model parameters, we conducted a series of tests on synthetic datasets that have the same back-azimuthal distribution as the observed fast directions. One test explores the case in which two-layer anisotropy has the same mean model parameters as the model that best fits the data, but the parameters are allowed to vary about those means following a Gaussian distribution with a standard deviation of 30° for a-axis azimuth, 10° for a-axis plunge, and 10% for anisotropy strength. This

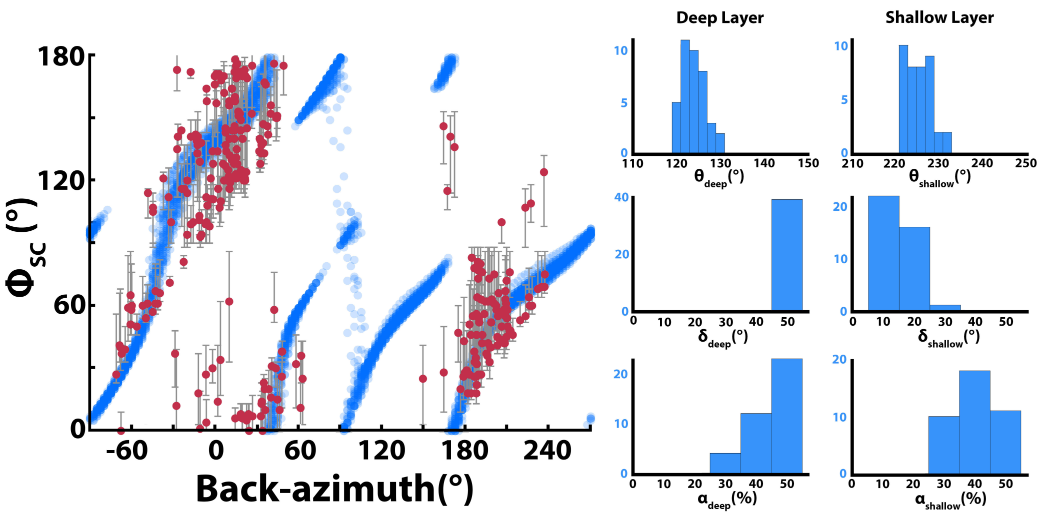

Figure 5. Left panel: suite of best-fitting model predictions of fast axis variation (blue) as a function of back-azimuth, obtained from the fine grid searches that satisfy the misfit criterion corresponding to the F-test at 95% confidence level, overlain on the fast-axis measurements from this study (red). Right panels: Histograms of the model parameters satisfying the misfit criterion.

case is intended to represent deformation as a function of depth which is similar across Greenland, but which varies laterally to a moderate degree. From this distribution of model parameters, a set of model parameters was drawn and fast directions were predicted for each back-azimuth in the real dataset for 50 different draws of model parameters. To generate the synthetic dataset, at every back-azimuth, we draw a value from one of the 50 different fast axis predictions. The model which best fits the synthetic dataset was then determined using the coarse grid of model parameter predictions. One of the 100 iterations is shown in Fig. 6a. This process was repeated 100 times, and the resulting distribution of best-fitting model parameters is in shown in Fig. 6c-h (blue histograms) together with the input distribution of model parameters (pink histograms). The retrieved model parameters are broadly similar to the input distribution of model parameters, in particular for the upper and lower layer a-axis azimuths which are the best resolved model parameters. This result supports the argument that meaningful anisotropy parameters can be retrieved from fast direction data, even when the underlying model varies moderately.

In a second test, the possibility that sub-regions have simpler single-layer anisotropy is added to the first scenario. In this test, 50% of the 50 model parameter sets come from the Gaussian distributions about the best-fitting two-layer model (as in Fig. 6a) and 50% are drawn from a distribution of one-layer anisotropy models. In the one-layer model distribution, horizontal a-axis azimuths have means of 50° and 115°, each with a standard deviation of 15°. Again, the process is repeated 100 times, and the resulting best-fitting model parameters are shown in Fig. 6i-n. Although the introduction of the one-layer models produces larger differences between the retrieved (blue) and input (pink) two-layer model parameter distributions, the retrieved a-axis azimuths fall within the input distribution. This result indicates that retrieved two-layer a-axis azimuths can be obtained not only when the underlying model varies moderately, but also when the regional dataset also reflects sub-regions that contain one-layer anisotropy.

Additional synthetic tests are described in the supplement (Figs. S5-S7 and Text S1). These tests include a scenario in which the fast directions at each back-azimuth are randomly drawn from the total distribution of fast directions (Fig. S7). This test is equivalent to assuming that each synthetic fast direction represents a localized region of one-layer anisotropy, and that any apparent pattern of fast direction with back-azimuth is coincidental. For 100 versions of this case, the resulting distribution of retrieved two-layer models contain model parameters across the range of possible values, and a-axis azimuth ranges for each layer are not well-constrained. These results fundamentally differ from those produced by fitting the observed fast directions. We conclude that the observed pattern of fast-direction versus back-azimuth in Greenland is not coincidental, and that two-layer anisotropy (or at least depth-varying anisotropy) is required.

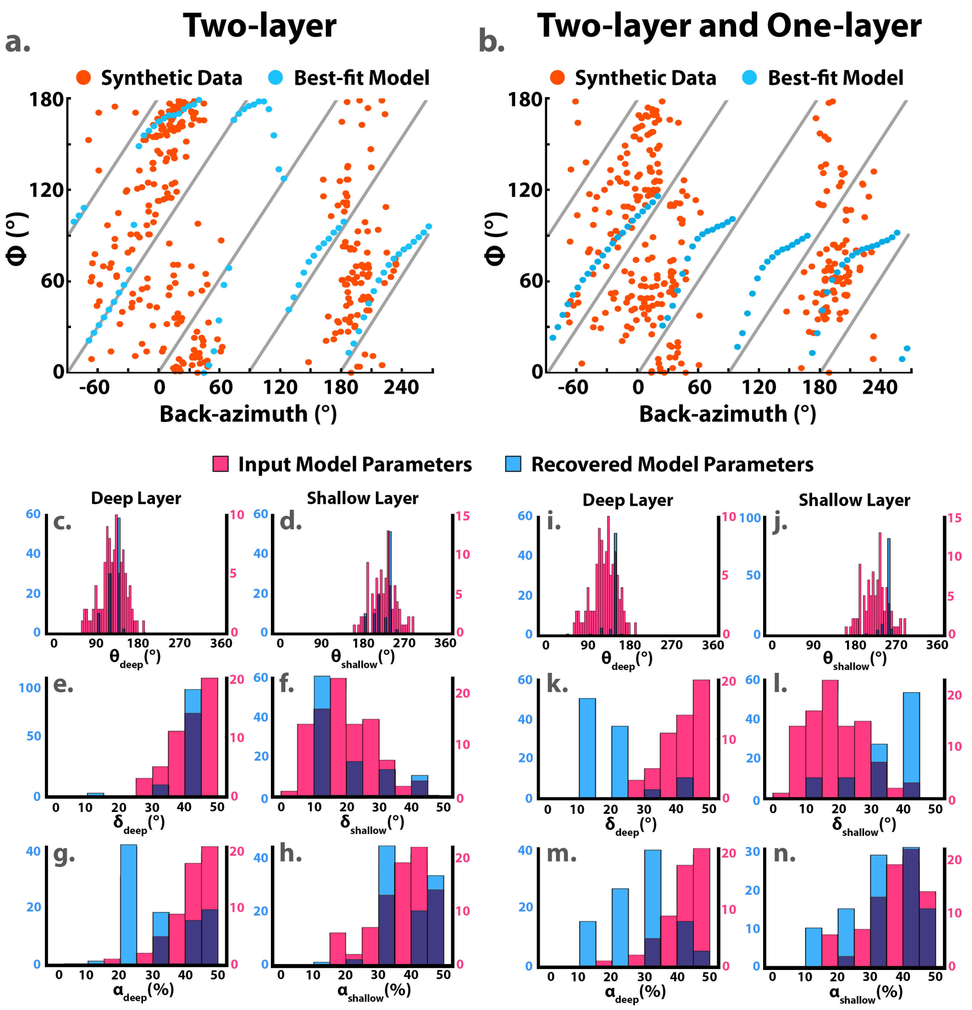

Figure 6. Synthetic test that explores how moderate random variation in two-layer model parameters impacts recovery of their distribution, without (a, c-h) and with (b, i-n) additional one-layer anisotropy. (a) One example of synthetic data (orange points) that are predictions of an input model where parameters are drawn from a Gaussian distributions where the mean is from the best-fitting model for the observed Greenland fast directions. Predictions of the retrieved model (blue) that best fits the synthetic data. (c-h) Distributions of model parameters recovered from fitting synthetic data (blue bars) for 100 cases of model parameters (pink bars) drawn from a Gaussian distribution where the mean is from the best-fitting model for the observations. (b) One example of synthetic data (orange points) that are predictions of a set of input models where 50% are drawn from a Gaussian distributions as described in (a) and 50% are drawn from one-layer models. (i-n) Distributions of model parameters recovered from fitting synthetic data (blue bars) for 100 cases of model parameters (pink bars) as described in (b).

4 Discussion

4.1 Comparison to Prior Studies of Anisotropy

Previous work in Greenland has suggested that significant differences in crustal azimuthal anisotropy exist between northern and southern Greenland (Darbyshire et al., 2018). However, we do not find any significant difference in the back-azimuthal pattern of fast directions between these regions (Fig. 3b). We also do not detect a difference in the pattern for stations on the Greenland ice sheet versus those on the coast. Although ice is an anisotropic mineral, the likely contribution to total splitting observed should be small, especially because there is likely not a coherent fabric throughout an entire column of ice within the ice sheet (e.g. Bentley, 1972; Harland et al., 2013; Smith et al., 2017; Thorsteinsson et al., 1997; Thorsteinsson, 2000).

The widespread coherence of back-azimuthal fast direction variation across the entirety of Greenland is a key feature of our results. Comparison of shear-wave splitting measurements from some previous studies in Greenland and the Canadian high arctic (Dubé et al., 2020; Helffrich et al., 1994) indicates broad agreement (Fig. 7) with the back-azimuthal dependence of the fast direction observed here. However, the fast direction distribution with back-azimuth from Ucisik et al. (2008) is less similar. Strong fast direction variations with back-azimuth were found in some studies from other regions of the Canadian shield (Fig. S3), but differences in these patterns relative to those in this study suggest regional variations in anisotropic parameters (Bastow et al., 2011; Darbyshire et al., 2015; Liddell et al., 2017; Snyder et al., 2013).

Among published models of azimuthal anisotropy, the regional models based on group velocity from Darbyshire et al. (2018) provide information at lateral scales most comparable to our results. At shallow mantle depths, Darbyshire et al. (2018) indicate NE-SW fast directions in the far north and south of Greenland, which are consistent with a-axis azimuths in the lithospheric layer of the best-fitting models found here, and NW-SE fast direction beneath the central latitudes of Greenland, which do not agree with our lithospheric parameters. However, the Darbyshire et al. (2018) group velocity results indicate weak anisotropy at mantle depths and represent constraints on only the shallow lithospheric mantle, leaving open the possibility that the two studies are compatible.

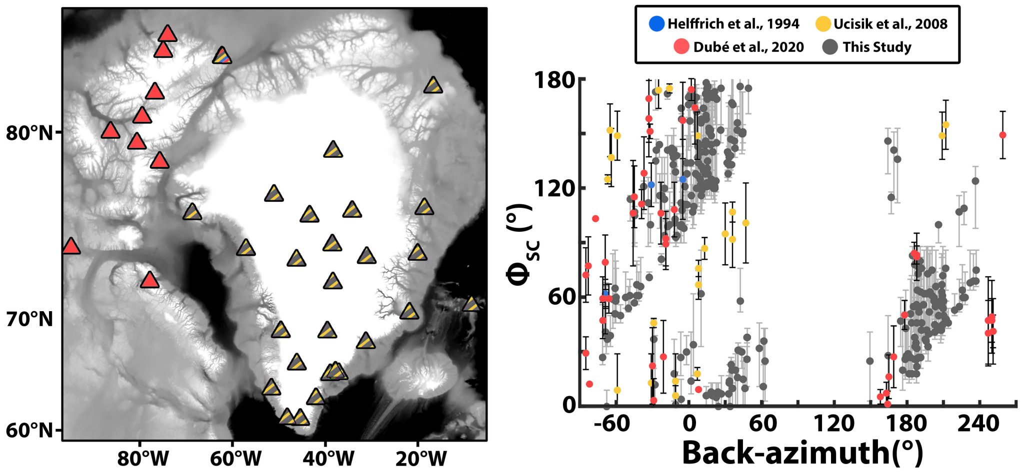

Figure 7. Left: Locations of stations outside of and in Greenland used in certain other studies. Colors are the same in the map and back-azimuth plot. Right: Comparison of our shear wave splitting fast polarizations (gray) with the results from other studies. $N_{otherstudies} = 70$.

4.2 Interpretation of Two-layer Anisotropy Models in Terms of Mantle Deformation

A simple, first-order prediction for shear in the asthenosphere is that it would be driven by absolute plate motion, resulting in olivine a-axis azimuths that are parallel to absolute plate motion. Olivine a-axes in the deeper layer of the two-layer anisotropy models that provide acceptable fits to the observed Greenland fast directions (120° to 130°) are approximately aligned with absolute plate motion in Greenland assuming the no-net-rotation reference frame plate motion model of Argus et al. (2011).

Consistency of asthenospheric a-axes azimuths and plate motion shear differs from the conclusions of some previous studies of anisotropy (Darbyshire et al., 2015; Liddell et al., 2017). These studies assert that asthenospheric anisotropy parallel to plate motion should not be expected, because the North American plate speed (∼20 mm/yr) is slower than what is required (∼40 mm/yr) to develop basal drag fabric (Debayle & Ricard, 2013). However, the 40 mm/yr threshold (Debayle & Ricard, 2013) refers to whole-plate alignment of fabric with plate motion. Indeed, Debayle and Ricard (2013) state that for slow moving continental plates, the correlation between asthenospheric fabric and plate motion is more complicated, but that agreement can persist over large scales, citing central and eastern North America as an example. Thus, when considering a study region which is smaller than an entire plate, slow plate velocities do not rule out asthenospheric fabric in agreement with plate motion, either from basal drag or secondary convection (Debayle & Ricard, 2013).

We also compared the parameters of the deeper layer of anisotropy to models of mantle flow that account for mantle temperature, buoyancy and viscosity, as well plate motion boundary conditions. However, due to different boundary conditions and other model assumptions, predictions for asthenospheric flow directions beneath Greenland differ between studies, and it is possible to find models which are broadly consistent with the acceptable a-axes found here (Conrad & Behn, 2010; Marquart et al., 2007) or inconsistent (e.g. Colli et al., 2018; Conrad & Behn, 2010; Marquart et al., 2007; Mihalffy et al., 2008).

The agreement between our well-constrained deep layer a-axis fast azimuths and the no-net-rotation plate motion directions from Argus et al. (2011) make a strong case for asthenospheric anisotropy produced by shearing due to plate motion. However, the fact that acceptable a-axis plunges are $\sim 50°$ pose a complication for this model. Even though a-axis plunge is less well-resolved than a-axis azimuth in the two-layer modeling, models with near-horizontal lower layer a-axes produce significantly worse fits to the observed fast polarization directions. The apparent a-axis plunges suggest vertical flow components, for example due to asthenosphere diverted beneath Greenland's thick cratonic lithosphere or at the edges of a potential channel of thin lithosphere created by the thermal signature of the Iceland hotspot (Fig. 8).

The relationship between the shallow layer a-axis azimuths inferred from the modeling (222° to 232°) and lithospheric deformation fabrics is difficult to evaluate because the Greenland ice sheet occludes much of the geologic evidence typically used to compare lithospheric anisotropy fabrics with the deformation signatures of major tectonic events. Nonetheless, inferred a-axis azimuths are consistent with deformation fabrics from Proterozoic and Archean orogenic events in western and northern Greenland. The Trans-Hudson Orogeny, which occurred 1.8 Ga, is responsible for Greenland's prominent Nagssugtoqidian belt, although the direction of compression and shape of the tectonic boundary is obscured by the ice sheet and has been interpolated many ways across Greenland (Antonijevic & Lees, 2018; Dawes, 2009; Henriksen et al., 2009; Pourpoint et al., 2018). Unobscured by the ice sheet, shear zones in Western Greenland closely associated with

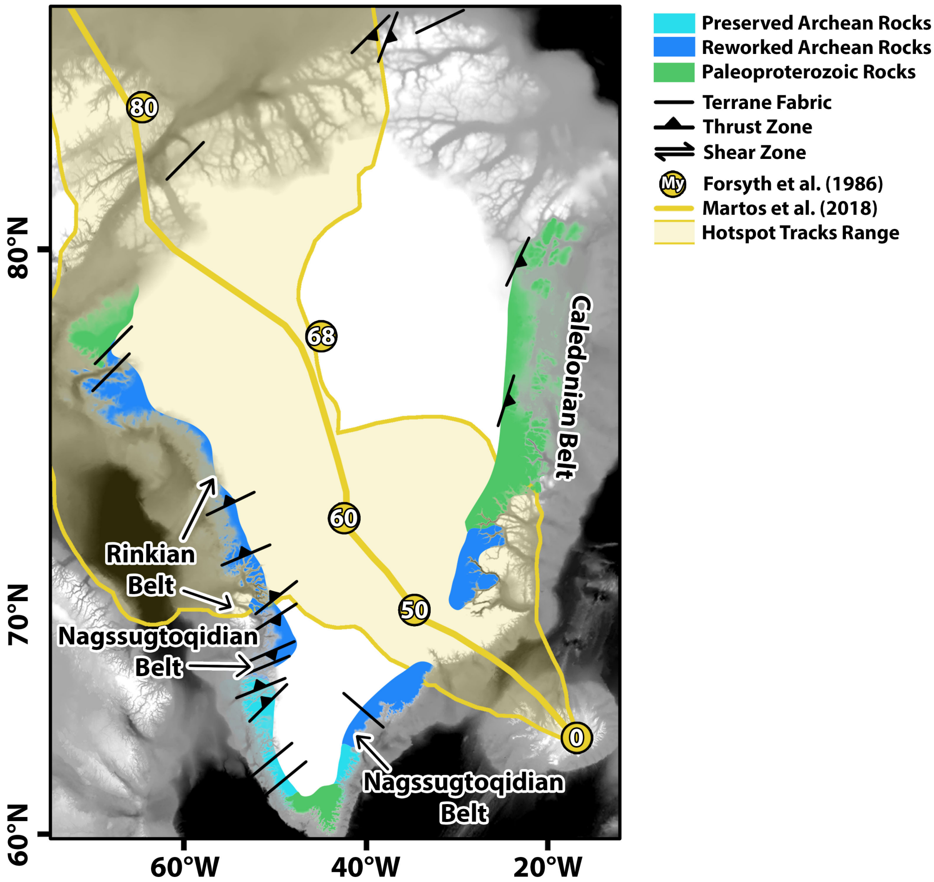

Figure 8. Map of relevant geology and tectonic features. Underlying gray field is ETOPO1 topography (Amante & Eakins, 2009) with basement ages, terrane fabrics, thrust zones, and orogenic belts from Henriksen et al. (2009); Dawes (2009); Higgins and Leslie (2000) Van Gool et al., (2002), Sanborn-Barrie et al. (2017), and Van Gosen and Piepjon (1999). The yellow-shaded region represents the extent of previously proposed hotspot tracks as compiled in Martos et al. (2018); the bold yellow line is their proposed hotspot track. Numbers show hotspot surface projections at different times from Forsyth et al. (1986).

the Nagssugtoqidian orogen trend ENE-WSW to NE-SW (van Gool et al., 2002; Bak et al., 1975), parallel to local thrust zones and older Archean terranes (van Gool et al., 2002; Henriksen et al., 2009; Korstgård et al., 1987). NW-directed thrusting has also been inferred in the Proterozoic Rinkian orogen to the north in western Greenland (Sanborn-Barrie et al., 2017; van Gool et al., 2002), and in thrust zones at Greenland's northern margin (Von Gosen & Piepjohn, 1999). These indicators of lithospheric deformation are consistent with acceptable a-axis azimuths from the two-layer anisotropy modeling, and this agreement suggests that similarly-oriented deformation fabrics are also present beneath the ice sheet.

However, deformation indicators in eastern Greenland are less consistent with the overall NE-SW acceptable lithospheric a-axis orientations. In southeastern Greenland, van Gool et al. (2002) infer an ESE structural grain. At two stations within this zone (ANGG and KULG), fast directions are predominantly NW-SE, raising the possibility that lithospheric deformation in this zone is rotated from the shallow layer trend indicated by the modeling of the complete set of Greenland stations. In addition, thrust fronts in the Paleozoic Greenland Caledonides are oriented ∼N-S (Dawes, 2009). This inconsistency with the overall NE-SW oriented shallow layer a-axis orientation may reflect an unresolved local variation in lithospheric a-axis alignment, or that lithospheric fabric associated with the Caledonian orogeny was limited in its depth extent, possibly due to decoupling of the Laurentian retro-lithosphere (Hodges, 2016).

Local deformation associated with rifting has impacted both eastern and western Greenland at differing scales. The orientation of extension associated with Labrador sea rifting in the west is parallel to the shallow layer a-axis orientations, and strong crustal anisotropy associated with mineral alignment during this process is resolved by Clement et al. (1994) via shear-wave splitting. On the other hand, local rifting basins in East Greenland show W-E and NW-SE extension (Henriksen et al., 2009), the latter being perpendicular to the shallow a-axis orientations inferred here. This discrepancy may not be significant if orogenic deformation over longer length-scales dominates lithospheric fabrics, relative to more localized rifting events.

By comparing SKS and SKKS measurements, Dubé et al. (2020) show that anisotropy in the lower mantle impacts measurements at station ALE. Lower mantle anisotropy has been imaged below Iceland and shown to impact differential SKS-SKKS measurements at Greenland stations (Wolf et al., 2019). We did not resolve consistent discrepancies between SKS and SKKS splitting in our dataset (Fig. S4). Nonetheless, further work should be conducted to constrain the extent to which anisotropy from lower mantle or crustal sources (e.g. Clement et al., 1994) may impact the shear-wave splitting measurements in this study.

5 Conclusions

Using 299 new splitting measurements from stations across Greenland, we have found a consistent pattern of fast direction variation in back-azimuth which indicates the presence of multi-layer anisotropy. We used grid searches to solve for two-layer models of anisotropy that provide acceptable fits to the fast directions. Acceptable a-axis azimuths are 222° to 232° in the shallow layer, and 120° to 130° in the deep layer.

The modeling results are consistent with an interpretation where anisotropy in the deeper layer represents asthenospheric shearing due to plate motion in a no-net-rotation reference frame. The upper layer is consistent with lithospheric anisotropy due to Proterozoic and Archean orogenic events, as indicated by tectonic fabrics in western and northern Greenland. The strong variations in back-azimuthal pattern of fast directions in Greenland, combined with prior work in the Canadian high arctic, are consistent with coherent lithospheric deformation from Proterozoic and Archean orogenesis on a broader scale than previously appreciated.

Acknowledgments

We thank reviewers [TBD] for feedback. We thank all the operators involved for their work in servicing and deploying the stations in Greenland we used, including network codes DK (the Danish Seismological Network), GE (GEOFON, doi:10.14470/TR560404), XF (the temporary GLISN network, https://doi.org/10.7914/SN/XF_2014), G (GEOSCOPE, doi:10.18715/GEOSCOPE.G), CN (Canadian National Seismograph Network, https://doi.org/10.7914/SN/CN) and II (the IRIS/IDA Global Seismographic Network, https://doi.org/10.7914/SN/II). Seismic data used can be downloaded from the IRIS DMC and GEOFON data archives. We thank Isabella Gama, Hannah Krueger, Julia Krogh, and Ningli Zhao for assistance with making initial measurements. Some figures were prepared with GMT software (Wessel and Smith, 1995). A.H is supported by an NSF Graduate Research Fellowship under grant DGE-16-44760.

References

Abt, D. L., & Fischer, K. M. (2008). Resolving three-dimensional anisotropic structure with shear wave splitting tomography. *Geophysical Journal International*, *173*(3), 859–886.

Abt, D. L., Fischer, K. M., Abers, G. A., Protti, M., González, V., & Strauch, W. (2010). Constraints on upper mantle anisotropy surrounding the cocos slab from sk (k) s splitting. *Journal of Geophysical Research: Solid Earth*, *115*(B6).

Abt, D. L., Fischer, K. M., Abers, G. A., Strauch, W., Protti, J. M., & González, V. (2009). Shear wave anisotropy beneath nicaragua and costa rica: Implications for flow in the mantle wedge. *Geochemistry, Geophysics, Geosystems*, *10*(5).

Amante, C., & Eakins, B. W. (2009). Etopo1 arc-minute global relief model: procedures, data sources and analysis.

Antonijevic, S. K., & Lees, J. M. (2018). Effects of the iceland plume on greenland's lithosphere: New insights from ambient noise tomography. *Polar Science*, *17*, 75–82.

Aragon, J. C., Long, M. D., & Benoit, M. H. (2017). Lateral variations in sks splitting across the magic array, central appalachians. *Geochemistry, Geophysics, Geosystems*, *18*(11), 4136–4155.

Argus, D. F., Gordon, R. G., & DeMets, C. (2011). Geologically current motion of 56 plates relative to the no-net-rotation reference frame. *Geochemistry, Geophysics, Geosystems*, *12*(11).

Bak, J., Korstgård, J., & Sørensen, K. (1975). A major shear zone within the nagssugtoqidian of west greenland. *Tectonophysics*, *27*(3), 191–209.

Bastow, I. D., Thompson, D. A., Wookey, J., Kendall, J.-M., Helffrich, G., Snyder, D. B., ... Darbyshire, F. A. (2011, jan). Precambrian plate tectonics: Seismic evidence from northern Hudson Bay, Canada. *Geology*, *39*(1), 91–94. doi: 10.1130/G31396.1

Bentley, C. R. (1972). Seismic-wave velocities in anisotropic ice: A comparison of measured and calculated values in and around the deep drill hole at byrd station, antarctica. *Journal of Geophysical Research*, *77*(23), 4406–4420.

Braun, A., Kim, H. R., Csatho, B., & von Frese, R. R. (2007). Gravity-inferred crustal thickness of greenland. *Earth and Planetary Science Letters*, *262*(1-2), 138–158.

Calixto, F. J., Robinson, D., Sandvol, E., Kay, S., Abt, D., Fischer, K., ... Alvarado, P. (2014, nov). Shear wave splitting and shear wave splitting tomography of the southern Puna plateau. *Geophysical Journal International*, *199*(2), 688–699. doi: 10.1093/gji/ggu296

Clement, W. P., Carbonell, R., & Smithson, S. B. (1994, apr). Shear-wave splitting in the lower crust beneath the Archean crust of southwest Greenland. *Tectonophysics*, *232*(1-4), 195–210. doi: 10.1016/0040-1951(94)90084-1

Colli, L., Ghelichkhan, S., Bunge, H. P., & Oeser, J. (2018). Retrodictions of Mid Paleogene mantle flow and dynamic topography in the Atlantic region from compressible high resolution adjoint mantle convection models: Sensitivity to deep mantle viscosity and tomographic input model. *Gondwana Research*, *53*, 252–272. doi: 10.1016/j.gr.2017.04.027

Conrad, C. P., & Behn, M. D. (2010). Constraints on lithosphere net rotation and asthenospheric viscosity from global mantle flow models and seismic anisotropy. *Geochemistry, Geophysics, Geosystems*, *11*(5). doi: 10.1029/2009GC002970

Dahl-Jensen, T., Larsen, T. B., Woelbern, I., Bach, T., Hanka, W., Kind, R., ... Gudmundsson, O. (2003). Depth to moho in greenland: receiver-function analysis suggests two proterozoic blocks in greenland. *Earth and Planetary Science*

Letters, *205*(3-4), 379–393.

Darbyshire, F. A., Bastow, I. D., Forte, A. M., Hobbs, T. E., Calvel, A., Gonzalez-Monteza, A., & Schow, B. (2015, dec). Variability and origin of seismic anisotropy across eastern Canada: Evidence from shear wave splitting measurements. *Journal of Geophysical Research: Solid Earth*, *120*(12), 8404–8421. doi: 10.1002/2015JB012228

Darbyshire, F. A., Dahl-Jensen, T., Larsen, T. B., Voss, P. H., & Joyal, G. (2018). Crust and uppermost-mantle structure of greenland and the northwest atlantic from rayleigh wave group velocity tomography. *Geophysical Journal International*, *212*(3), 1546–1569.

Dawes, P. R. (2009). The bedrock geology under the inland ice: the next major challenge for greenland mapping. *Geological Survey of Denmark and Greenland (GEUS) Bulletin*, *17*, 57–60.

Debayle, E., & Ricard, Y. (2013). Seismic observations of large-scale deformation at the bottom of fast-moving plates. *Earth and Planetary Science Letters*, *376*, 165–177. doi: 10.1016/j.epsl.2013.06.025

Dubé, J.-M., Darbyshire, F. A., Liddell, M. V., Stephenson, R., & Oakey, G. (2020). Seismic anisotropy of the canadian high arctic: Evidence from shear-wave splitting. *Tectonophysics*, *789*, 228524.

Ekström, G. (2011). A global model of love and rayleigh surface wave dispersion and anisotropy, 25-250 s. *Geophysical Journal International*, *187*(3), 1668–1686.

Fischer, K. M., Parmentier, E., Stine, A. R., & Wolf, E. R. (2000). Modeling anisotropy and plate-driven flow in the tonga subduction zone back arc. *Journal of Geophysical Research: Solid Earth*, *105*(B7), 16181–16191.

Forsyth, D., Morel-AL'Huissier, P., Asudeh, I., & Green, A. (1986). Alpha ridge and iceland-products of the same plume? *Journal of Geodynamics*, *6*(1-4), 197–214.

Hammond, J. O., Kendall, J.-M., Wookey, J., Stuart, G., Keir, D., & Ayele, A. (2014). Differentiating flow, melt, or fossil seismic anisotropy beneath ethiopia. *Geochemistry, Geophysics, Geosystems*, *15*(5), 1878–1894.

Harland, S., Kendall, J.-M., Stuart, G., Lloyd, G., Baird, A., Smith, A., … Brisbourne, A. (2013). Deformation in rutford ice stream, west antarctica: measuring shear-wave anisotropy from icequakes. *Annals of Glaciology*, *54*(64), 105–114.

Helffrich, G., Silver, P., & Given, H. (1994, nov). Shear-wave splitting variation over short spatial scales on continents. *Geophysical Journal International*, *119*(2), 561–573. doi: 10.1111/j.1365-246X.1994.tb00142.x

Henriksen, N., Higgins, A., Kalsbeek, F., & Pulvertaft, T. C. R. (2009). Greenland from archaean to quaternary. *Geological Survey of Denmark and Greenland Bulletin*, *18*, 126.

Higgins, A., & Leslie, A. (2000). Restoring thrusting in the east greenland caledonides. *Geology*, *28*(11), 1019–1022.

Hodges, K. (2016). Crustal decoupling in collisional orogenesis: Examples from the east greenland caledonides and himalaya. *Annual Review of Earth and Planetary Sciences*, *44*, 685–708.

Holtzman, B., Kohlstedt, D. L., Zimmerman, M. E., Heidelbach, F., Hiraga, T., & Hustoft, J. (2003). Melt segregation and strain partitioning: Implications for seismic anisotropy and mantle flow. *Science*, *301*(5637), 1227–1230.

Hung, S.-H., & Forsyth, D. W. (1998). Modelling anisotropic wave propagation in oceanic inhomogeneous structures using the parallel multidomain pseudo-spectral method. *Geophysical Journal International*, *133*, 726–740.

Karato, S.-i., Jung, H., Katayama, I., & Skemer, P. (2008). Geodynamic significance of seismic anisotropy of the upper mantle: new insights from laboratory studies. *Annu. Rev. Earth Planet. Sci.*, *36*, 59–95.

Korstgård, J., Ryan, B., & Wardle, R. (1987). The boundary between proterozoic and archaean crustal blocks in central west greenland and northern labrador. *Geological Society, London, Special Publications*, *27*(1), 247–259.

Kumar, P., Kind, R., Hanka, W., Wylegalla, K., Reigber, C., Yuan, X., ... others (2005). The lithosphere–asthenosphere boundary in the north-west atlantic region. *Earth and Planetary Science Letters*, *236*(1-2), 249–257.

Kumar, P., Kind, R., Priestley, K., & Dahl-Jensen, T. (2007). Crustal structure of iceland and greenland from receiver function studies. *Journal of Geophysical Research: Solid Earth*, *112*(B3).

Lawver, L. A., & Muller, R. D. (1994). Iceland hotspot track. *Geology*, *22*(4), 311–314.

Lebedev, S., Schaeffer, A. J., Fullea, J., & Pease, V. (2018). Seismic tomography of the arctic region: inferences for the thermal structure and evolution of the lithosphere. *Geological Society, London, Special Publications*, *460*(1), 419–440.

Levin, V., Menke, W., & Park, J. (1999). Shear wave splitting in the appalachians and the urals: a case for multilayered anisotropy. *Journal of Geophysical Research: Solid Earth*, *104*(B8), 17975–17993.

Levshin, A., Ritzwoller, M., Barmin, M., Villasenor, A., & Padgett, C. (2001). New constraints on the arctic crust and uppermost mantle: surface wave group velocities, pn, and sn. *Physics of the Earth and Planetary Interiors*, *123*(2-4), 185–204.

Levshin, A., Shen, W., Barmin, M., & Ritzwoller, M. (2017). Surface wave studies of the greenland upper lithosphere using ambient seismic noise. *Pure Appl. Geophys*, *174*.

Liddell, M. V., Bastow, I., Darbyshire, F., Gilligan, A., & Pugh, S. (2017). The formation of Laurentia: Evidence from shear wave splitting. *Earth and Planetary Science Letters*, *479*, 170–178. doi: 10.1016/j.epsl.2017.09.030

Long, M. D., & Becker, T. W. (2010). Mantle dynamics and seismic anisotropy. *Earth and Planetary Science Letters*, *297*(3-4), 341–354.

Long, M. D., De Hoop, M. V., & Van Der Hilst, R. D. (2008). Wave-equation shear wave splitting tomography. *Geophysical Journal International*, *172*(1), 311–330.

Mainprice, D., & Silver, P. G. (1993). Interpretation of sks-waves using samples from the subcontinental lithosphere. *Physics of the Earth and Planetary Interiors*, *78*(3-4), 257–280.

Marquart, G., Schmeling, H., & Čadek, O. (2007). Dynamic models for mantle flow and seismic anisotropy in the north atlantic region and comparison with observations. *Geochemistry, Geophysics, Geosystems*, *8*(2). doi: 10.1029/2006GC001359

Martos, Y. M., Jordan, T. A., Catalán, M., Jordan, T. M., Bamber, J. L., & Vaughan, D. G. (2018). Geothermal Heat Flux Reveals the Iceland Hotspot Track Underneath Greenland. *Geophysical Research Letters*, *45*(16), 8214–8222. doi: 10.1029/2018GL078289

Mihalffy, P., Steinberger, B., & Schmeling, H. (2008). The effect of the large-scale mantle flow field on the Iceland hotspot track. *Tectonophysics*, *447*(1-4), 5–18.

doi: 10.1016/j.tecto.2006.12.012

Mondal, P., & Long, M. D. (2020). Strong seismic anisotropy in the deep upper mantle beneath the cascadia backarc: Constraints from probabilistic finite-frequency sks splitting intensity tomography. *Earth and Planetary Science Letters*, *539*, 116172.

Mordret, A. (2018). Uncovering the iceland hot spot track beneath greenland. *Journal of Geophysical Research: Solid Earth*, *123*(6), 4922–4941.

Pourpoint, M., Anandakrishnan, S., & Ammon, C. J. (2018). High-resolution rayleigh wave group velocity variation beneath greenland. *Journal of Geophysical Research: Solid Earth*, *123*(2), 1516–1539.

Sanborn-Barrie, M., Thrane, K., Wodicka, N., & Rayner, N. (2017). The laurentia–west greenland connection at 1.9 ga: new insights from the rinkian fold belt. *Gondwana Research*, *51*, 289–309.

Savage, M. K., & Silver, P. G. (1993). Mantle deformation and tectonics: constraints from seismic anisotropy in the western united states. *Physics of the Earth and Planetary Interiors*, *78*(3-4), 207–227.

Schaeffer, A., Lebedev, S., & Becker, T. (2016). Azimuthal seismic anisotropy in the earth's upper mantle and the thickness of tectonic plates. *Geophysical Supplements to the Monthly Notices of the Royal Astronomical Society*, *207*(2), 901–933.

Servali, A., Long, M. D., Park, J., Benoit, M. H., & Aragon, J. C. (2020). Love-to-rayleigh scattering across the eastern north american passive margin. *Tectonophysics*, *776*, 228321.

Silver, P. G., & Chan, W. W. (1991). Shear wave splitting and subcontinental mantle deformation. *Journal of Geophysical Research: Solid Earth*, *96*(B10), 16429–16454.

Silver, P. G., & Savage, M. K. (1994). The interpretation of shear-wave splitting parameters in the presence of two anisotropic layers. *Geophysical Journal International*, *119*(3), 949–963.

Smith, E. C., Baird, A. F., Kendall, J. M., Martín, C., White, R. S., Brisbourne, A. M., & Smith, A. M. (2017). Ice fabric in an antarctic ice stream interpreted from seismic anisotropy. *Geophysical Research Letters*, *44*(8), 3710–3718.

Snecdecor, G. W., & Cochran, W. G. (1991). *Statistical methods.* John Wiley &

Sons.

Snyder, D. B., Berman, R. G., Kendall, J. M., & Sanborn-Barrie, M. (2013). Seismic anisotropy and mantle structure of the Rae craton, central Canada, from joint interpretation of SKS splitting and receiver functions. *Precambrian Research*, *232*, 189–208. doi: 10.1016/j.precamres.2012.03.003

Steffen, R., Audet, P., & Lund, B. (2018). Weakened lithosphere beneath greenland inferred from effective elastic thickness: A hot spot effect? *Geophysical Research Letters*, *45*(10), 4733–4742.

Steinberger, B., & Becker, T. W. (2018). A comparison of lithospheric thickness models. *Tectonophysics*, *746*, 325–338.

Steinberger, B., Bredow, E., Lebedev, S., Schaeffer, A., & Torsvik, T. H. (2019). Widespread volcanism in the greenland–north atlantic region explained by the iceland plume. *Nature Geoscience*, *12*(1), 61–68.

St-Onge, M. R., Van Gool, J. A., Garde, A. A., & Scott, D. J. (2009). Correlation of archaean and palaeoproterozoic units between northeastern canada and western greenland: constraining the pre-collisional upper plate accretionary history of the trans-hudson orogen. *Geological Society, London, Special Publications*, *318*(1), 193–235.

Thorsteinsson, T. (2000). *Anisotropy of ice ih: Developement of fabric and effects of anisotropy on deformation.*

Thorsteinsson, T., Kipfstuhl, J., & Miller, H. (1997). Textures and fabrics in the grip ice core. *Journal of Geophysical Research: Oceans*, *102*(C12), 26583–26599.

Toyokuni, G., Matsuno, T., & Zhao, D. (2020). P-wave tomography beneath greenland and surrounding regions—i. crust and upper mantle. *Journal of Geophysical Research: Solid Earth*, *n/a*(n/a), e2020JB019837. (e2020JB019837 2020JB019837) doi: 10.1029/2020JB019837

Ucisik, N., Gudmundsson, Ó., Hanka, W., Dahl-Jensen, T., Mosegaard, K., & Priestley, K. (2008). Variations of shear-wave splitting in greenland: Mantle anisotropy and possible impact of the iceland plume. *Tectonophysics*, *462*(1-4), 137–148.

Ucisik, N., Gudmundsson, Ó., Priestley, K., & Larsen, T. B. (2005). Seismic anisotropy beneath east greenland revealed by shear wave splitting. *Geo-*

physical research letters, *32*(8).

van Gool, J. A., Connelly, J. N., Marker, M., & Mengel, F. C. (2002). The nagssugtoqidian orogen of west greenland: tectonic evolution and regional correlations from a west greenland perspective. *Canadian Journal of Earth Sciences*, *39*(5), 665–686.

Vinnik, L., Makeyeva, L., Milev, A., & Usenko, A. Y. (1992). Global patterns of azimuthal anisotropy and deformations in the continental mantle. *Geophysical Journal International*, *111*(3), 433–447.

Von Gosen, W., & Piepjohn, K. (1999). Evolution of the kap cannon thrust zone (north greenland). *Tectonics*, *18*(6), 1004–1026.

Wolf, J., Creasy, N., Pisconti, A., Long, M. D., & Thomas, C. (2019). An investigation of seismic anisotropy in the lowermost mantle beneath iceland. *Geophysical Journal International*, *219*(Supplement_1), S152–S166.

Wookey, J. (2012). Direct probabilistic inversion of shear wave data for seismic anisotropy. *Geophys. J. Int*, *189*, 1025–1037. doi: 10.1111/j.1365-246X.2012.05405.x

Wüstefeld, A., Bokelmann, G., Zaroli, C., & Barruol, G. (2008). Splitlab: A shear-wave splitting environment in matlab. *Computers & Geosciences*, *34*(5), 515–528.

Yuan, H., & Levin, V. (2014). Stratified seismic anisotropy and the lithosphere-asthenosphere boundary beneath eastern north america. *Journal of Geophysical Research: Solid Earth*, *119*(4), 3096–3114.

Supporting Information for "Multi-layer Seismic Anisotropy Beneath Greenland"

Erica Nathan[1,2], Anant Hariharan[1,2], Darien Florez[1], Karen M. Fischer[1]

[1]Department of Earth, Environmental, and Planetary Sciences, Brown University, Providence, RI, USA

[2]These authors contributed equally to this work.

Contents of this file

1. Text S1
2. Figures S1 to S7

Additional Supporting Information (Files uploaded separately)

1. Table S1: Information about stations used in this study.
2. Table S2: Individual splitting measurements used in this study.

,

Introduction

Text S1 explains the methods for the synthetic tests of parameter recovery with uneven back-azimuthal sampling.

Table S1 shows information about each of the 27 stations used in the final dataset. Table S2 presents each individual splitting measurement used in the final dataset. Table S1 and S2 are also accessible at the Brown Digital Data Repository: https://repository.library.brown.edu/studio/item/bdr:1149085/, https://doi.org/10.7910/DVN/XB4SCT

Figure S1 shows measurements of shear-wave splitting fast polarization directon as a function of back-azimuth for each of the individual stations contributing to the final set of splitting measurements used in this study. The corresponding figure for NEEM is also in the main text. Figure S2 shows measurements of delay times as a function of back-azimuth for all stations in this study. Figure S3 shows fast axis measurements from prior studies in adjacent regions of North America, in addition to those shown in Figure 7 of the main text. Figure S4 shows measurements of fast axis as a function of back-azimuth for all stations, grouped by the type of *KS phase. Figures S5-7 show results from synthetic tests that explore the recovery of model parameters corresponding to two layers of anisotropy for datasets constructed with different underlying distributions and sources/levels of noise.

Text S1.

Here, we describe the parameters and process for the synthetic tests shown in Figure 6 and S5-7 in more detail.

Goal of Synthetic Tests: The goal of these tests is to examine how recovery of model parameters is affected by the (i) starting model, (ii) sampling of multiple starting models, and (iii) the back-azimuthal sampling. To this end, we have conducted the following series of tests.

Test 1a (Fig. S5a, c-h): Can we recover the two-layer model from a sampling of two-layer models that vary only slightly? To construct the synthetic dataset for Test 1a, at every back-azimuth for which we have an observation of shear-wave splitting, we choose a predicted fast direction from the pool of 39 values that corresponds to the models that pass the F-test from the finer grid search. If the chosen fast direction is within 3° of the back-azimuth, it is eliminated, simulating the impact of avoiding null measurements. This test explores whether it is possible to recover a two-layer model from a sampling of two-layer models that vary slightly in their underlying model parameters. The recovered model parameters for the 100 tested cases overlap the distributions of input model parameters. This test shows that minor variations in underlying two-layer anisotropy do not inhibit meaningful retrieval of representative model parameters.

Test 1b (Fig. S5b, i-n): How much does additionally sampling from one or more single layer models affect the appearance of an otherwise consistent two-layer pattern? This test expands upon Test 1a by including the possibility that our synthetic dataset may sample a single layer of anisotropy in addition to the two-layer pattern. At every back-azimuth, there is a 50% chance that a measurement will sample one of the predictions corresponding to the F-test from the finer grid search, and a 50% chance that a measurement will sample a one-layer measurement drawn from one of two Gaussian distributions: one with a mean of 50° and a standard deviation of 30° and another with a mean of 115° and a standard deviation of 30°. If a measurement is within 10° of the corresponding back-azimuth, it is eliminated and a new measurement is chosen. Our calculations show that some retrieved models fall outside the distributions of input two-layer model parameters, which is not surprising since 50° of the data are now drawn from the "contaminating" one-layer models. However, the results of the grid search still resolve deep and shallow layer a-axis azimuths whose most likely values represent the two-layer distribution they are drawn from.

Test 2a (Fig. S6a, c-h): Does sampling from many different two-layer models yield a coherent result and, if so, is that result representative of any of the input models? This test explores whether grid search modeling of a synthetic dataset generated from two-layer model parameters with Gaussian distributions can retrieve the input two-layer distribution. This test is similar to that shown in Fig. 6 of the main text, except that the underlying distribution of model parameters is not related to that obtained from the grid search. The starting model distributions are given as:

- A shallow a-axis centered on a mean of 140°, with a standard deviation of 30°
- A deep a-axis centered on a mean of 180°, with a standard deviation of 30°
- A shallow dip centered on a mean of 40°, with a standard deviation of 10°
- A deep dip centered on a mean of 20°, with a standard deviation of 10°
- A shallow strength centered on a mean of 40%, with a standard deviation of 10%
- A deep strength centered on a mean of 40%, with a standard deviation of 10%

For 50 combinations of model parameters drawn from these distributions, a set of predictions are generated at the back-azimuths of the real dataset. To construct the final synthetic dataset, a value is drawn at every one of the back-azimuths from the suite of 50 model predictions. If the chosen value is within 10° of the corresponding back-azimuth, the draw is repeated to avoid a null measurement. We repeat this process 100 times, and thus conduct 100 coarse grid searches. The range of retrieved model parameters is similar to the input values. However, the introduction of the 30°, standard deviation on a-axis azimuth reduces the accuracy of model parameter retrieval. While the peak of recovered a-axes in the shallow layer in both cases is similar to the peak of the input distribution, the distributions of input and recovered a-axes in the deeper layer differ more.

Test 2b (Fig. S6b, i-n): How much does additionally sampling from one or more single layer models affect our ability to get a result from a sampling of multiple disparate two-layer models? This test adds the same Gaussian distribution around single layers as in Test 1b to the two-layer data in Test 2a, with 50% probability for drawing from the two-layer versus one-layer model predictions. As with the previous tests, this process is repeated 100 times. Comparisons of input and retrieved model parameter distributions are similar to those in Test 2a, with slightly larger differences.

Test 3 (Fig. S7): Can sampling multiple single layer models produce a grid search result that looks like a two-layer model? Test 3 assesses whether one-layer anisotropy, sampled randomly by different *KS paths, could produce an apparent pattern of fast direction with back-azimuth that results in well-constrained two-layer model parameters. The answer is no. In this test, at each back-azimuth in the real data, a fast direction is drawn at random from the distribution of our measured fast directions

(Fig. S7c). Fast directions within 10° of the back-azimuth are redrawn to avoid null measurements. We repeat this process 100 times, and conduct 100 coarse grid searches of the resulting synthetic fast directions. In contrast to the results of the previous tests, the resulting distribution of retrieved two-layer models contain model parameters across the range of possible values, and a-axis a-azimuth ranges for each layer are not well-constrained. From this test we conclude that the observed pattern of fast-direction versus back-azimuth in Greenland is not coincidental, and that two-layer anisotropy (or at least depth-varying anisotropy) is required.

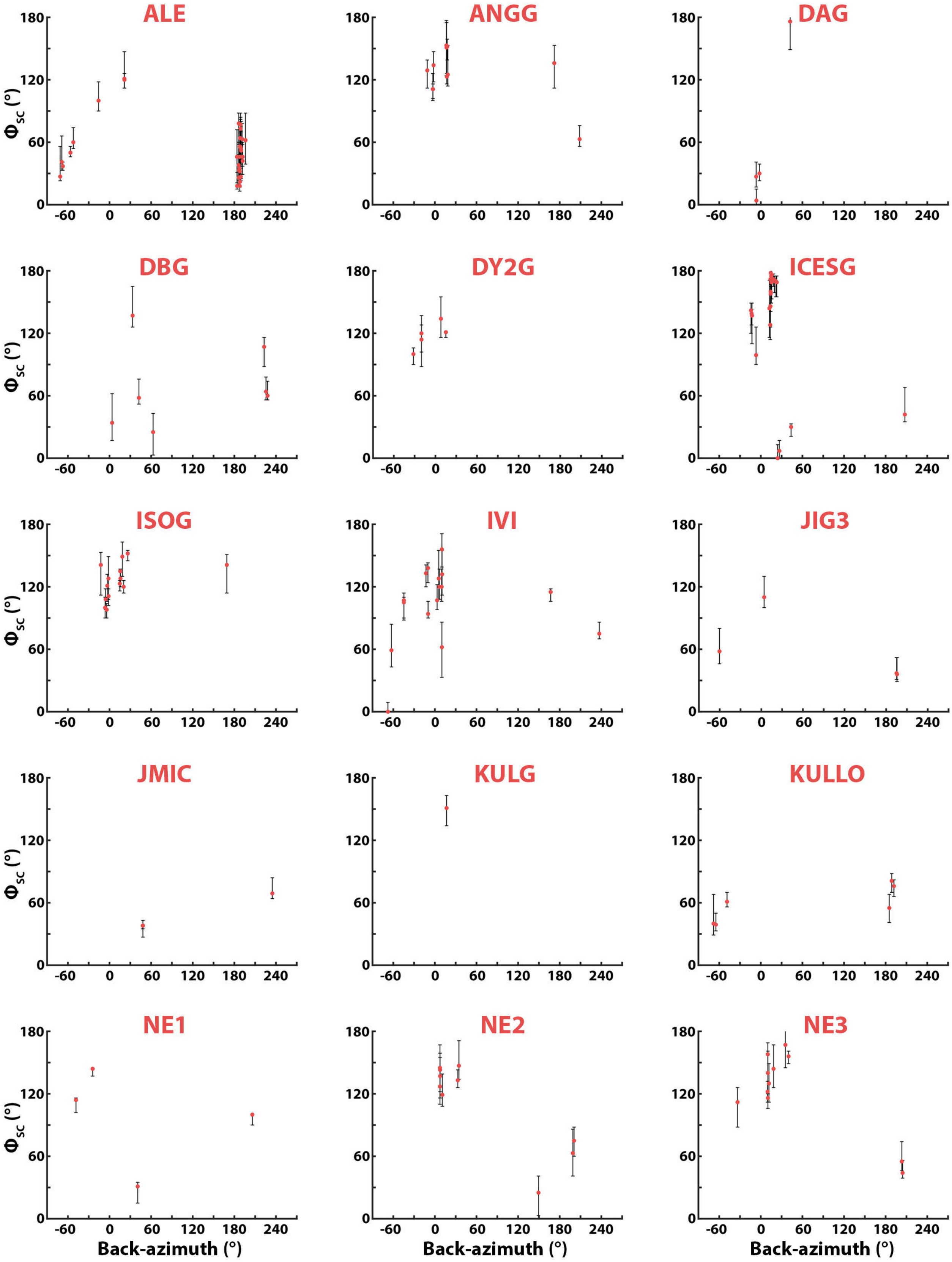

Figure S1a. Back-azimuthal variation of fast-axis measurements for all the stations used in this study, shown individually.

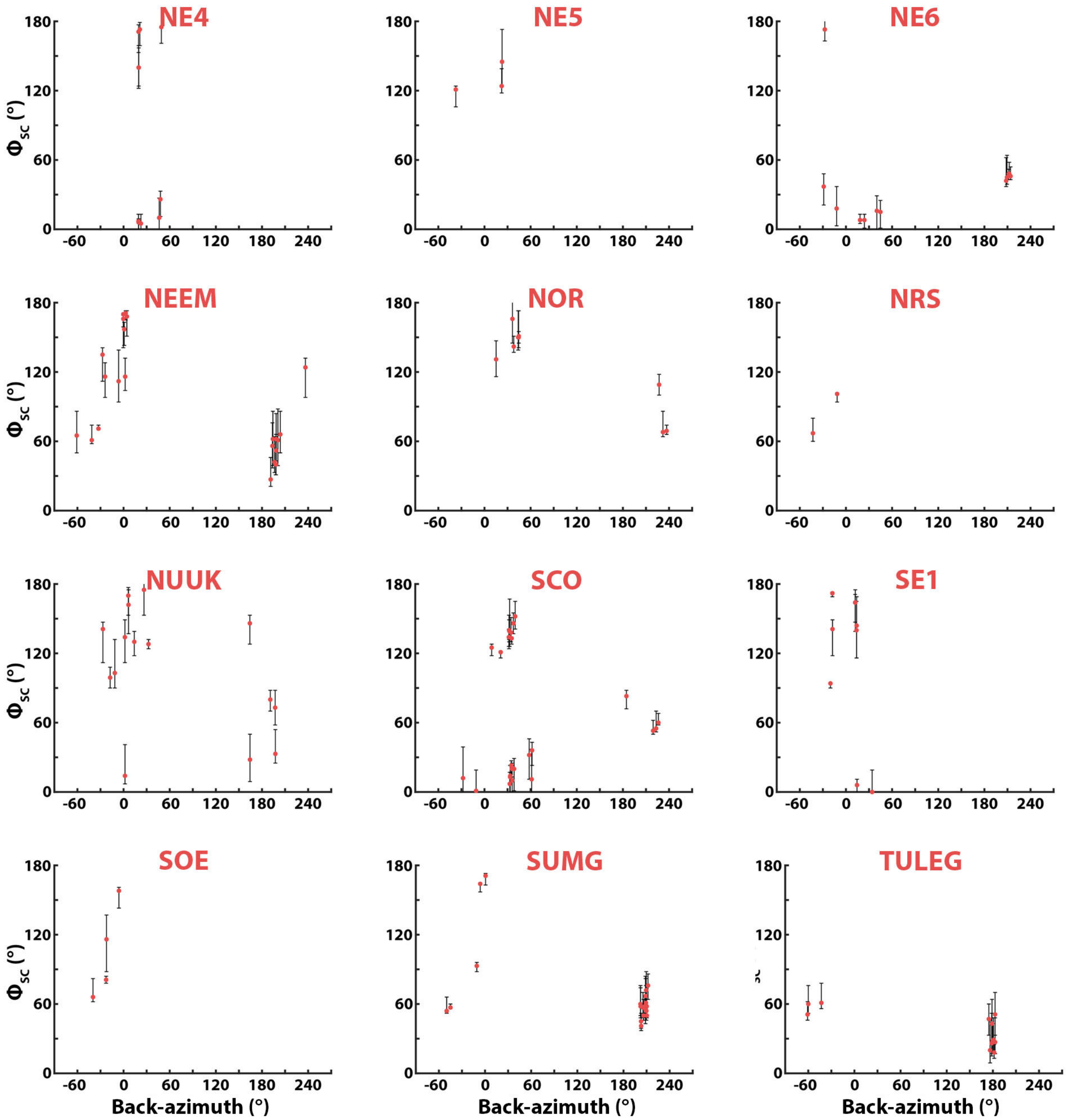

Figure S1b. Back-azimuthal variation of fast-axis measurements for all the stations used in this study, shown individually.

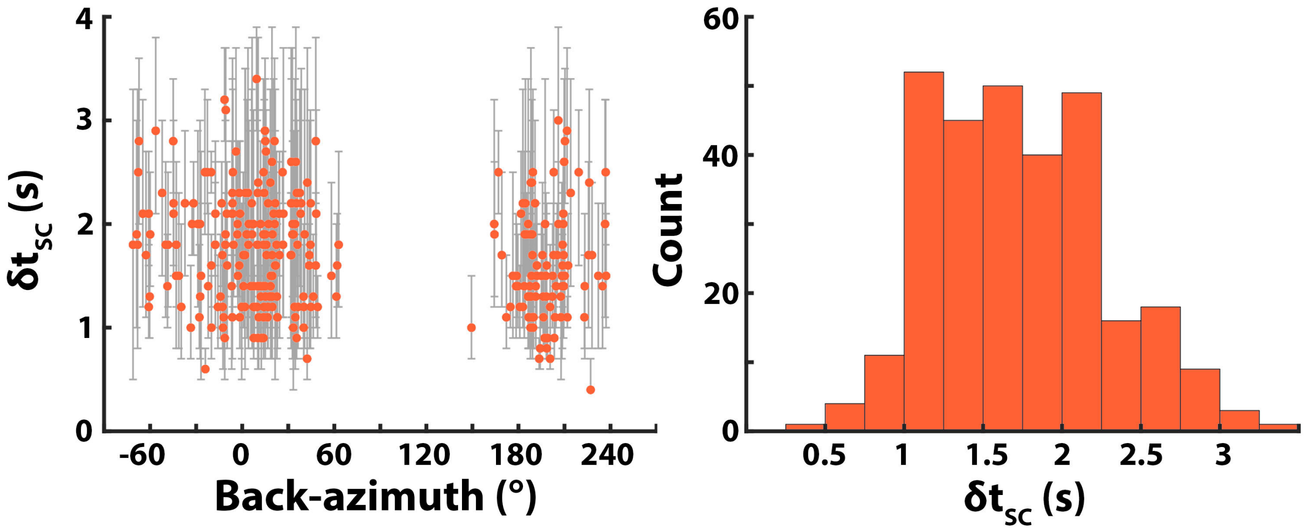

Figure S2. Back-azimuthal distribution of splitting delay times (left) and histogram showing distribution of delay times (right).

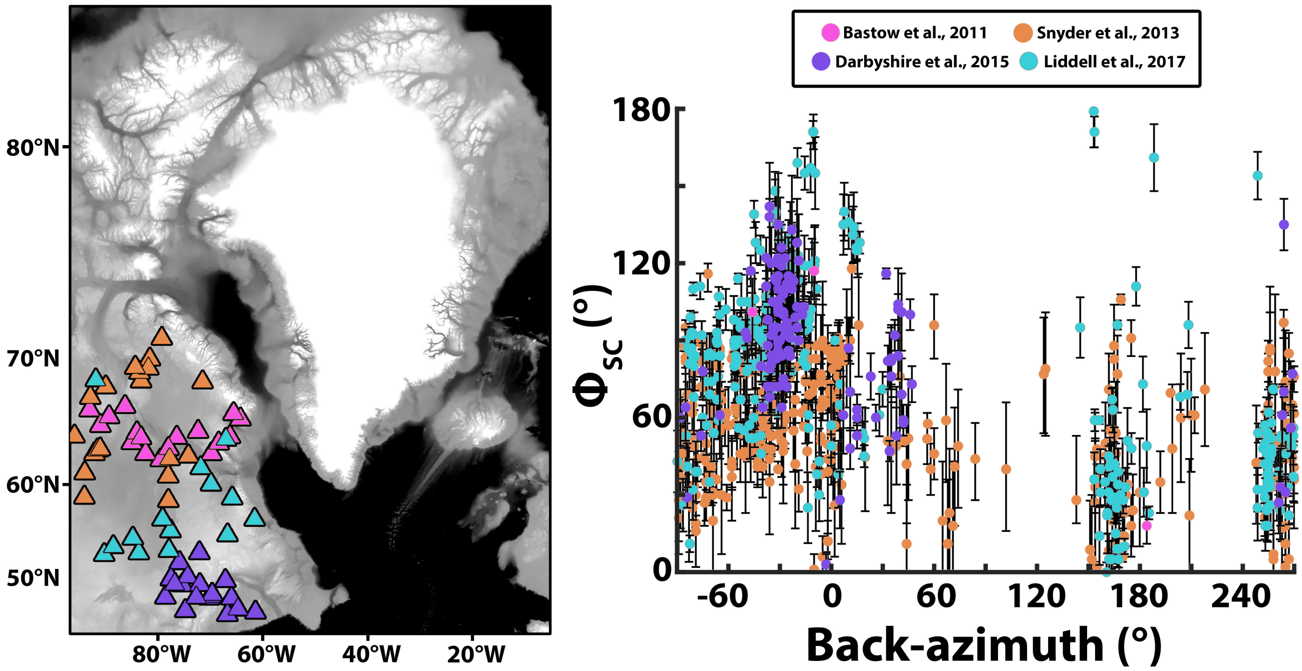

Figure S3. Left: Locations of stations outside of Greenland used in SKS splitting studies at locations somewhat geographically separated from Greenland. Colors are the same in the map and plot. Underlying map is topography. Right: Comparison of aggregate results from other studies.

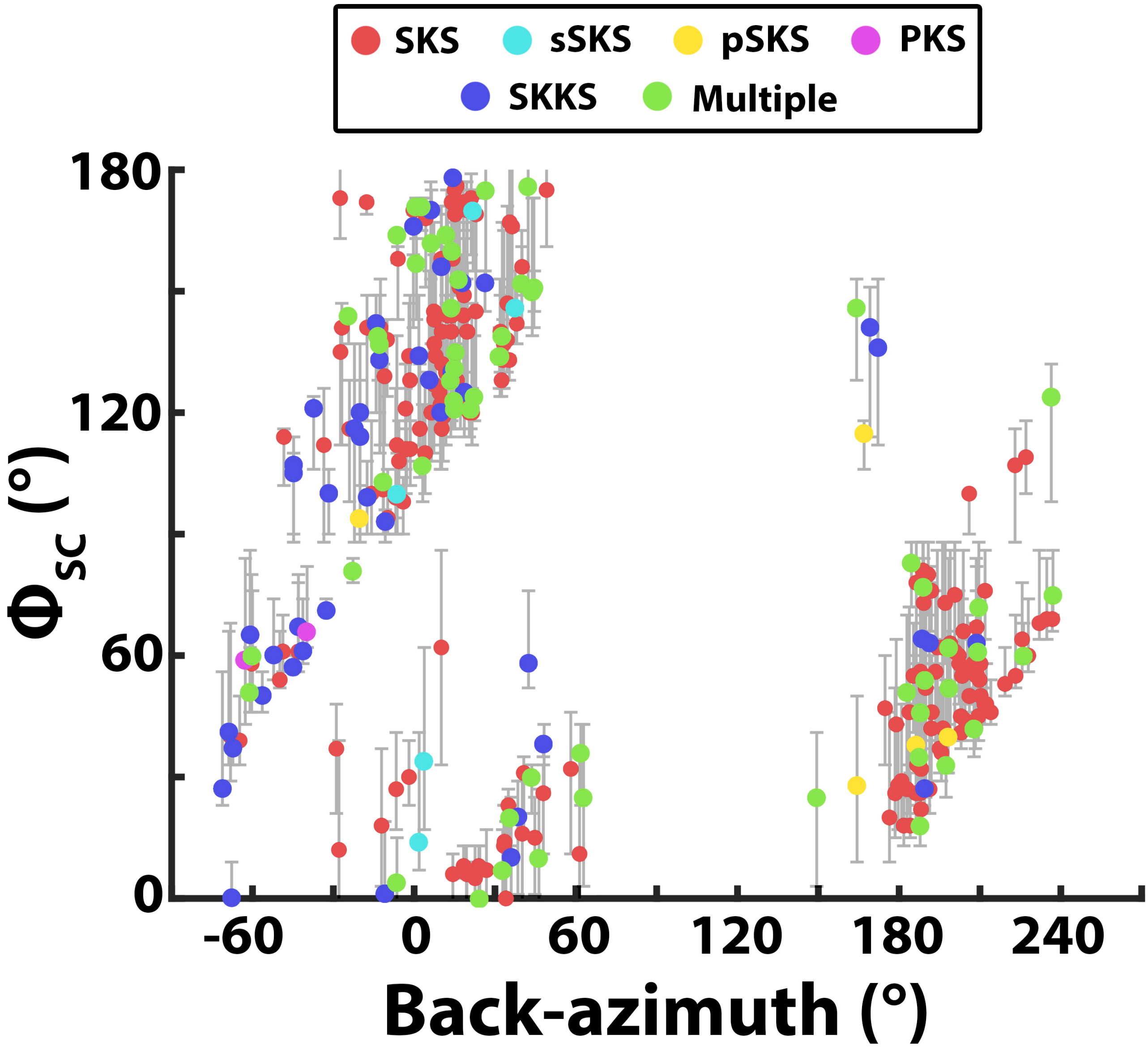

Figure S4. Back-azimuthal variation of fast axis measurements grouped by the phase the measurement was made on. A designation of "Multiple" indicates that multiple *KS phase arrivals were sufficiently close together that it was not possible to definitively say which phase the measurement was made on.

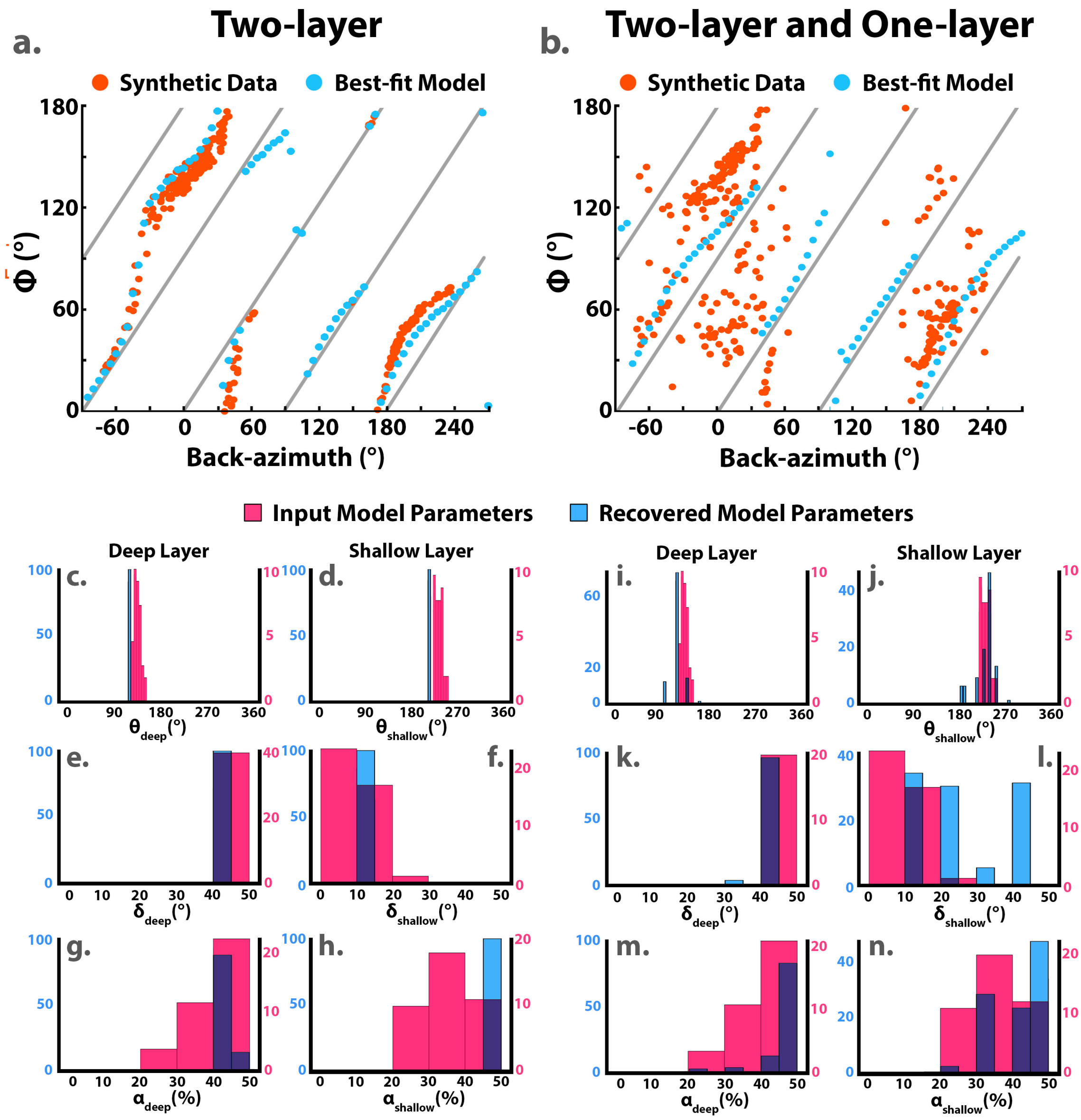

Figure S5. Figure S5. Results of synthetic tests exploring the impact of noise from 1-layer models. In Test 1a in panel (a), the synthetic fast direction at each back-azimuth is from one of the 39 two-layer models that pass the f-test from the fine gird search applied to the real data. In Test 1b in panel (b), the synthetic fast direction has a 50% chance at any back-azimuth to be drawn from the models in Test 1a, and 50% to be from a model with a single horizontal a-axis, with a-axis azimuths characterized as Gaussian distributions centered on either a mean of 50° or 115° , with a standard deviation of 30° . The synthetic data were modeled using the coarse grid of models applied to the real data. The recovered model parameters from 100 different realizations of these datasets are shown in panels (c-f) for Test 1a and (i-n) for Test 1b as blue bars, and the family of models used to generate the synthetic data are shown as pink bars.

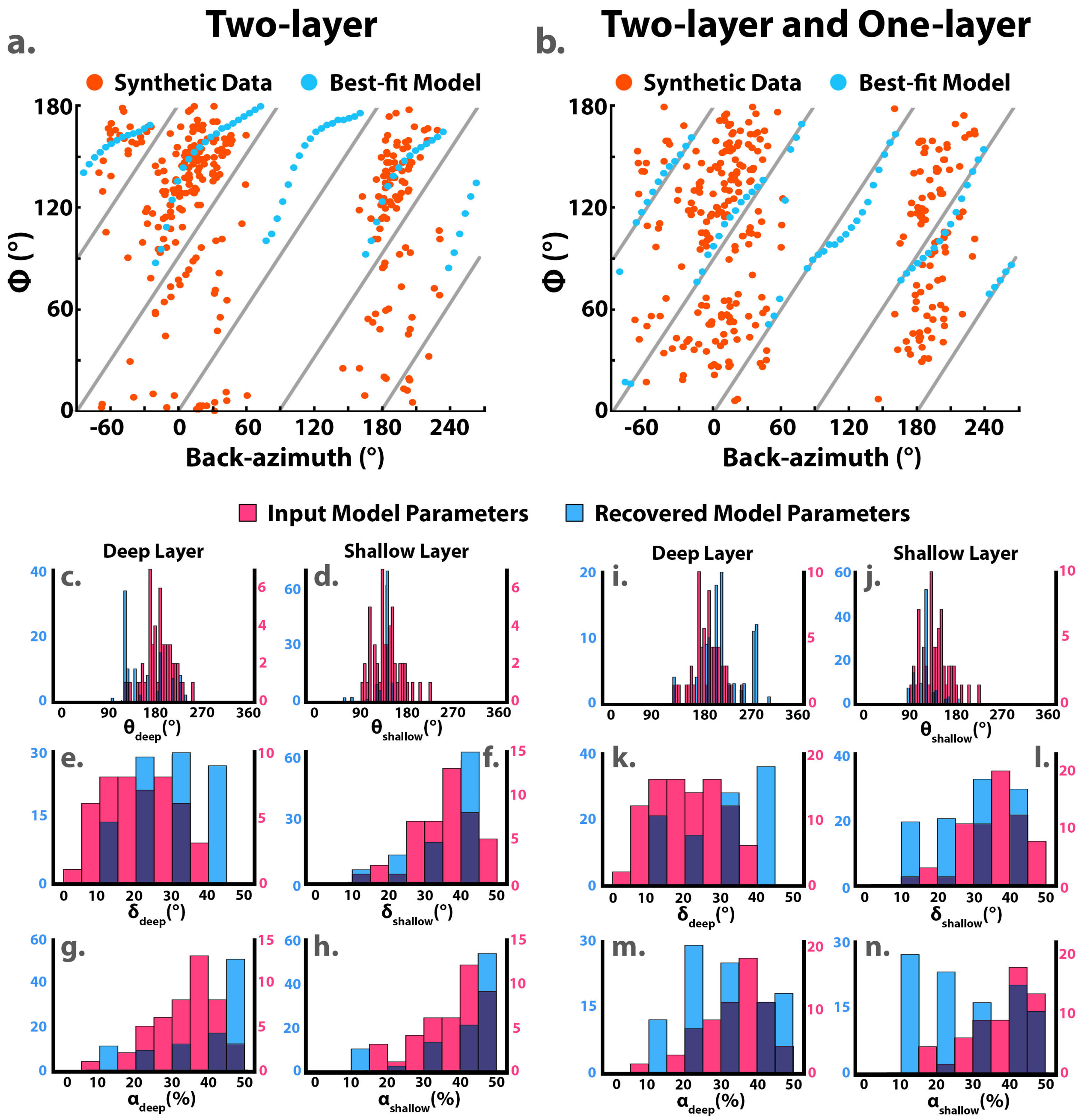

Figure S6. Synthetic test that explores how moderate random variation in two-layer model parameters impacts recovery of their distribution, without and with additional one-layer anisotropy. In Test 2a (a) this noise is due to an underlying Gaussian distribution on each of each of the six model parameters (Text S1). In Test 2b (b) the model distributions in (a) are further complicated by the addition of parameters from one-layer models, with Gaussian distributions as in Test 1b (Fig. S5b). The recovered model parameters from 100 different realizations of these datasets are shown in panels (c-f) for Test 2a and (i-n) for Test 2b as blue bars, and the family of models used to generate the synthetic data are shown as pink bars.

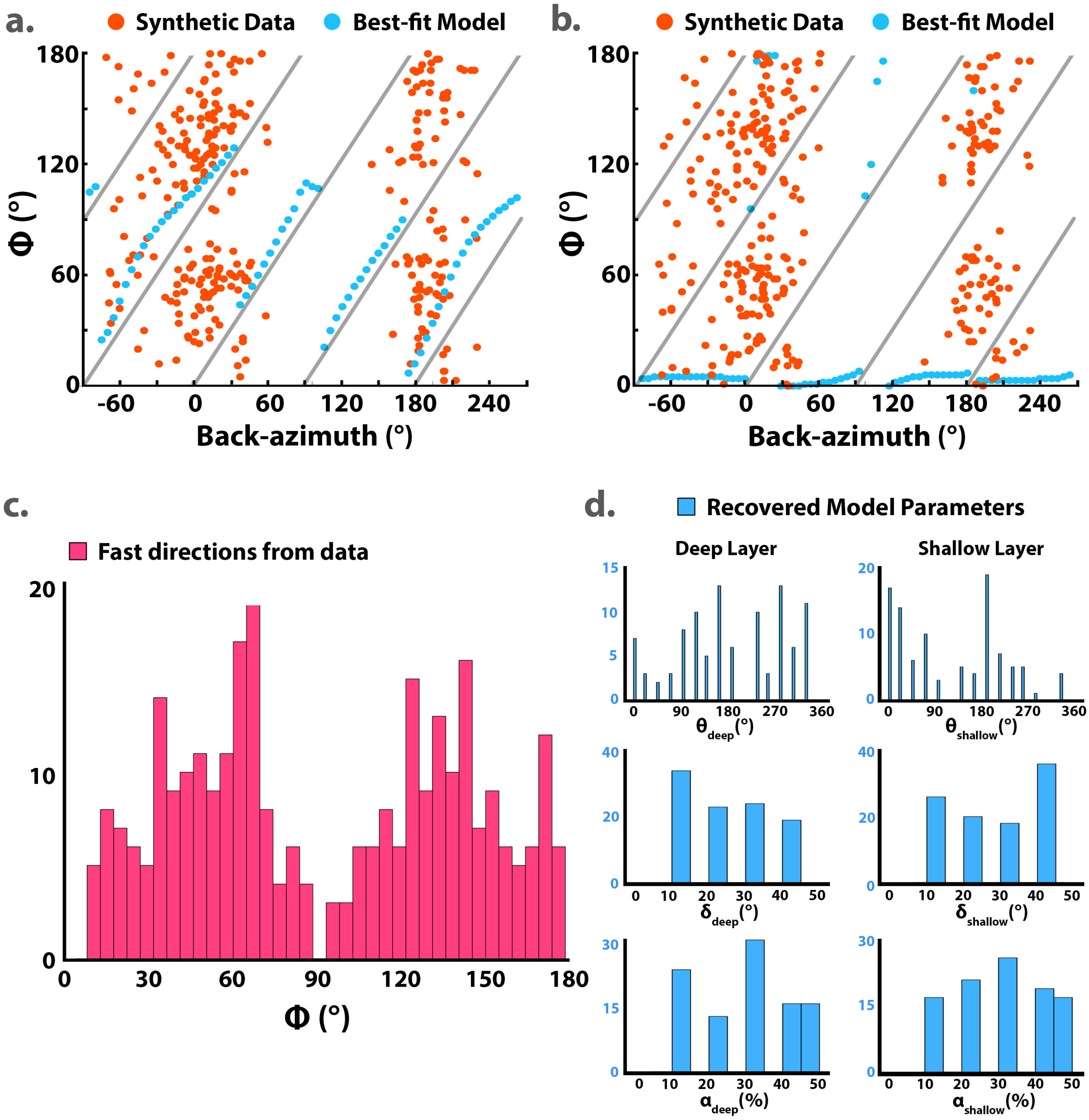

Figure S7. Synthetic tests with fast directions dataset that are drawn from a distribution of fast direction measurements that parallels the distribution of observed fast directions (See text S1). (a,b) Examples of realizations of the synthetic datasets we are fitting. (c) Distribution of our fast direction measurements, indicating the likelihood of any given fast direction in the synthetic dataset. (d) Distribution of recovered model parameters for grid searches on 100 synthetic datasets.

,